

## Evolution of the chiral rotation mode in rhodium isotopes

J. Peng<sup>1,\*</sup> and Q. B. Chen<sup>2,†</sup>

<sup>1</sup>*Department of Physics, Beijing Normal University, Beijing 100875, China*

<sup>2</sup>*Department of Physics, East China Normal University, Shanghai 200241, China*



(Received 30 January 2022; accepted 25 March 2022; published 19 April 2022)

Self-consistent solutions for the chiral rotation in the rhodium isotopes  $^{102-107}\text{Rh}$  are obtained within the three-dimensional tilted axis cranking covariant density functional theory. The orientation of angular momenta is determined self-consistently by minimizing the total Routhian surface calculations with respect to the azimuth angle  $\varphi$  and polar angle  $\theta$  for a given rotational frequency. It is found that when neutrons are added the critical rotational frequency  $\omega_{\text{crit}}$  of the appearance of chiral aplanar rotation decreases, which can be attributed to the neutrons in (*gd*) shells having smaller and larger angular momentum components along the short and medium axes, respectively. The theoretical results agree well with the experimental energy spectra, electromagnetic transition probabilities, as well as the kinetic and dynamic moments of inertia.

DOI: [10.1103/PhysRevC.105.044318](https://doi.org/10.1103/PhysRevC.105.044318)

### I. INTRODUCTION

Chirality is a well-known phenomenon existing commonly in nature, such as the spiral arm of the nebula, the spirals of snail shells, and the handedness of amino acids. In the atomic nucleus, chirality was suggested in a triaxially deformed nucleus with high-*j* valence particle(s) and hole(s) for the motion that the total angular momentum vector lies outside the three principal planes in the intrinsic frame (aplanar rotation) with left- or right-handed orientations [1]. The restoration of the spontaneous chiral symmetry breaking in the laboratory frame could give rise to the observation of the so-called chiral doublet bands, i.e., a pair of nearly degenerate  $\Delta I = 1$  bands with the same parity [1]. Normally the static chirality (or chiral rotation) exists only above a certain critical frequency of nuclear rotation  $\omega_{\text{crit}}$  [2]. Below the  $\omega_{\text{crit}}$ , the chiral vibrations, understood as the oscillation of the total angular momentum between the left- and the right-handed configurations in the body-fixed frame, exists. If multiple pairs of chiral doublet bands exist in a single nucleus, it corresponds to a new phenomenon of  $M\chi D$  [3], which provides evidence of triaxial shape coexistence.

After the pioneering work on the nuclear chiral rotation and  $M\chi D$ , lots of efforts have been made to understand these novel phenomena and explore the manifestations thereof in the nuclear chart. To date, more than 50 candidates for chiral rotation spreading in the mass regions  $A \approx 80$ ,  $A \approx 100$ ,  $A \approx 130$ , as well as  $A \approx 190$  have been reported, see, e.g., data tables [4]. These observations indicate that the nuclear chirality and multiple chirality are not restricted to a specific configuration in one nucleus or one mass region.

The main goal of the present paper is to investigate the chirality in the rhodium isotope chain in the  $A \approx 100$  mass region. In this isotope, several chiral candidates with the configurations of one proton hole in  $g_{9/2}$  orbital and one or two  $\nu h_{11/2}$  neutron particles have been reported. As the first example of chiral candidate in the  $A \approx 100$  mass region, a pair of chiral bands with asymmetrical configuration was identified in  $^{104}\text{Rh}$  in 2004 by Vaman *et al.* [5]. Subsequently, the existence of chiral doublet bands has been claimed in odd-odd  $^{106}\text{Rh}$  [6] as well as in odd-*A*  $^{103}\text{Rh}$  [7] and  $^{105}\text{Rh}$  [8,9]. In particular, lifetime measurements for candidates of chirality in  $^{102,103,104}\text{Rh}$  were performed and the behaviors of the obtained  $B(E2)$  and  $B(M1)$  transition probabilities were investigated [10,11]. Moreover,  $M\chi D$  with identical configuration [12–14] was further reported in  $^{103}\text{Rh}$  [15], which indicates that the chiral geometry in nuclei can be robust against the increase of the intrinsic excitation energy. So far, an island of nuclear chirality with about 20 candidates around  $^{104}\text{Rh}$  has been observed in the  $A \approx 100$  mass region [4].

On the theoretical side, several approaches were used to investigate the chirality in the rhodium isotopes. At the beginning, the three-dimensional tilted axis cranking (3D-TAC) based on the Strutinsky shell correction method with a hybrid of Woods-Saxon and Nilsson potentials [16,17] confirmed the chiral characters of two pairs of nearly degenerate doublet bands with different configurations in  $^{105}\text{Rh}$  [8,9]. Using a quantal triaxial particle-rotor model (PRM) with one-particle–one-hole coupled to a triaxial core, the candidate chiral doublet bands in  $^{104}\text{Rh}$  [18] and  $^{106}\text{Rh}$  [19] were investigated. By an updated *n*-particle–*n*-hole PRM, the chirality and the evolution of chiral geometry in  $^{103}\text{Rh}$  and  $^{105}\text{Rh}$  have been studied [20]. On the relativistic theory aspects, the adiabatic and configuration-fixed constrained CDFT was developed to investigate the triaxial shape coexistence [3]. Possible existence of  $M\chi D$  was predicted first for  $^{106}\text{Rh}$  [3] and later for neighboring nuclei [21–23]. Currently, the  $M\chi D$  has been

\*jpeng@bnu.edu.cn

†qbchen@phy.ecnu.edu.cn

verified experimentally in  $^{105}\text{Rh}$  [8,9] and  $^{103}\text{Rh}$  [15] in rhodium isotopes and in other nuclei [24–29].

In order to describe the chiral geometry microscopically, a 3D-TAC calculation is required and the CDFT has been extended to the case that the cranking axis could lie outside the three principal planes, i.e., the 3D-TAC CDFT [30]. Using the 3D-TAC CDFT, the chirality in  $^{106}\text{Rh}$  [30],  $^{106}\text{Ag}$  [31], and  $^{135}\text{Nd}$  [32] have been investigated. In these studies, the existence of the critical frequency  $\omega_{\text{cirt}}$  corresponding to the transition from planar to aplanar rotation is supported. For example, in Ref. [32], a classical Routhian was extracted by modeling the motion of the nucleons in rotating mean field as the interplay between the single-particle motions of several valence particle(s) and hole(s) and the collective motion of a core-like part. This classical Routhian gives qualitative agreement with the 3D-TAC CDFT result of  $\omega_{\text{cirt}}$ .

Therefore, the study of chirality in rhodium isotopes is a matter of general interest on both experimental and theoretical aspects. Such a wealth of data for chirality in rhodium isotope [5–11,15] encourages us to investigate therein three dimensional rotation and chirality, in particular the evolution of the critical frequency when neutrons are added, in a microscopic and self-consistent manner. One notes that the CDFT has played an important role in a fully microscopic and universal description for lots of nuclear phenomena [33–38]. In particular, for nuclear rotation, CDFT has been extended and used to describe superdeformed bands [39], magnetic rotations [40–45], antimagnetic rotations [44–48], as well as chiral rotations [3,21–23,30–32,45,49–51]. In this paper, following the similar procedures outlined in Refs. [30–32], we will focus on the evolution of three-dimensional rotation in  $^{102-107}\text{Rh}$  within 3D-TAC CDFT. The total Routhian curves, evolution of the orientation angles, spin-rotational frequency relationship, as well as the angular momentum contributions from  $(gd)^n$  shells in  $^{102-107}\text{Rh}$  will be investigated in detail. The calculated energy spectra and the electromagnetic transition probabilities will be compared with the experimental data.

## II. THEORETICAL FRAMEWORK

In the 3D-TAC CDFT [30–32], a nuclear rotating state is described by the Dirac equation in the intrinsic frame rotating with a constant angular velocity vector  $\boldsymbol{\omega}$ , pointing in an arbitrary direction in space:

$$[\boldsymbol{\alpha} \cdot (\mathbf{p} - \mathbf{V}) + \beta(m + S) + V - \boldsymbol{\omega} \cdot \hat{\mathbf{J}}]\psi_k = \epsilon_k \psi_k. \quad (1)$$

Here,  $\hat{\mathbf{J}} = \hat{\mathbf{L}} + \frac{1}{2}\hat{\boldsymbol{\Sigma}}$  is the total angular momentum of the nucleon spinors. The  $S$ ,  $V$ , and  $\mathbf{V}$  are the relativistic scalar field, the time-like component of vector field, and the space-like components of vector field, respectively, which are in turn coupled with the nucleon densities and current distributions. The Dirac equation is solved in a set of three-dimensional harmonic oscillator basis iteratively, and one finally obtains the single-nucleon spinors  $\psi_k$ , the single-particle Routhians  $\epsilon_k$ , the total energies, the expectation values of the angular momenta, transition probabilities, and so on. Using the semiclassical cranking condition  $\langle \hat{\mathbf{J}} \rangle \cdot \langle \hat{\mathbf{J}} \rangle = I(I + 1)$ , one can relate the magnitude of the angular velocity  $\boldsymbol{\omega}$  to the angular

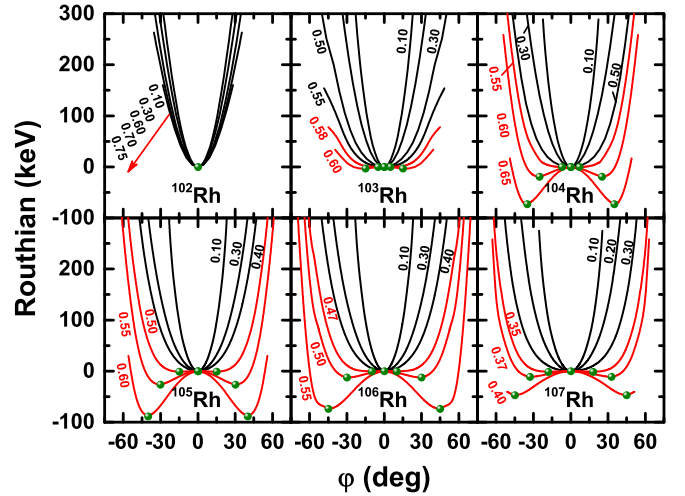


FIG. 1. Total Routhian curves as functions of the azimuth angle  $\varphi$  calculated by 3D-TAC CDFT for configurations  $\pi g_{9/2}^{-3} \otimes \nu [h_{11/2}^1 (gd)^n]$  in  $^{102-107}\text{Rh}$ . All curves are normalized at  $\varphi = 0$ . The minima of the curves are denoted by the green dots. The corresponding rotational frequencies are labeled by the the numbers given.

momentum quantum number  $I$ . Meanwhile, the orientation of  $\boldsymbol{\omega}$  is determined self-consistently by minimizing the total Routhian (cf. Fig. 1).

In the present work, we adopt the point-coupling density functional PC-PK1 [52] and employ a spherical harmonic oscillator basis with ten major shells to solve the Dirac equation. The pairing correlation is neglected in the calculations, but one has to bear in mind that the pairing correlation might have some influences on the descriptions of critical frequency [2,53] as well as the total angular momentum and  $B(M1)$  values [9,54,55].

## III. RESULTS AND DISCUSSION

As discussed above, the chiral candidates have been proposed in  $^{102-106}\text{Rh}$  in the previous works [5–11,15]. The valence protons and neutrons originate from the  $g_{9/2}$  and  $h_{11/2}$  subshells and two kinds of high- $j$  quasiparticle unpaired nucleon configurations  $\pi g_{9/2}^{-1} \otimes \nu h_{11/2}^1$  and  $\pi g_{9/2}^{-1} \otimes \nu h_{11/2}^2$  are assigned. It is therefore interesting to perform an examination of chirality within the framework of fully self-consistent theory and further study the evolution of chiral mode in the rhodium isotopes. Since the abundant data in  $^{102-106}\text{Rh}$  are available based on the configuration with one  $\nu h_{11/2}$  particle, only the bands with unpaired nucleon configuration  $\pi g_{9/2}^{-1} \otimes \nu h_{11/2}^1$  are considered here. Therefore, in the present study for  $^{102-107}\text{Rh}$ , there is a neutron always occupying at the bottom of the  $h_{11/2}$  shell. In the calculations, the occupation of the valence protons in the  $g_{9/2}$  shell and the valence neutrons in the  $h_{11/2}$  shell are fixed by tracing the single particle levels with increasing frequencies, while other nucleons are treated self-consistently by filling the orbitals according to their energies from the bottom of the well. Note that the neutrons above  $N = 50$  shell closure are distributed over the  $(gd)$  shell. Meanwhile, three proton holes are located at the top of the  $g_{9/2}$

shell, but two of them are antialigned. In this way, the valence nucleon configurations  $\pi g_{9/2}^{-3} \otimes \nu[h_{11/2}^1(gd)^n]$  ( $n = 6, 7, 8, 9, 10$ , and  $11$ ) are yielded for  $^{102-107}\text{Rh}$  and are similar to those in earlier studies in Refs. [5–8,10,11,15].

In the TAC calculations, the orientation of the angular velocity  $\omega$  with respect to the principal axis of the density distribution should be determined in a self-consistent way either by minimizing the total Routhian or by requiring that  $\omega$  is parallel with the total angular momentum  $\mathbf{J}$  at a fixed  $\omega$  value. Here, the polar angle  $\theta$  and azimuth angle  $\varphi$  are used to denote the orientation of the angular velocity  $\omega = \omega(\sin\theta \cos\varphi, \sin\theta \sin\varphi, \cos\theta)$ . The  $\theta$  is the angle between the angular velocity  $\omega$  and the long ( $l$ ) axis, while  $\varphi$  is the angle between the projection of  $\omega$  onto the short-medium ( $sm$ ) plane and the short ( $s$ ) axis. One notes that the sign of  $\varphi$  can be used to characterize the chirality of the rotating system [56]. Hence, the total Routhians curves of  $^{102-107}\text{Rh}$  for several rotational frequencies  $\hbar\omega$  are shown as functions of  $\varphi$  in Fig. 1 for configurations  $\pi g_{9/2}^{-3} \otimes \nu[h_{11/2}^1(gd)^n]$ , which is obtained by minimizing the total Routhian with respect to the polar angle  $\theta$  for each given azimuthal angle  $\varphi$ .

As expected, all the Routhian curves are symmetrical with respect to the  $\varphi = 0$  line since the two chiral configurations with  $\pm|\varphi|$  for a given  $\theta$  are of identical energy. On the whole, the Routhian curves are rather steep at low rotational frequency  $\omega$  and the minima appear at  $\varphi = 0$  that corresponds to a planar rotation in the  $sl$  plane for the yrast band. With increasing  $\hbar\omega$ , the curves become softer with respect to  $\varphi$  before the onset of two minima in a limited range of rotational frequency. The limited rotational frequency corresponds to the so-called critical frequency  $\omega_{\text{crit}}$  of chiral rotation [2,53], which are  $\hbar\omega_{\text{crit}} = 0.58, 0.55, 0.49, 0.46$ , and  $0.34$  MeV for  $^{103-107}\text{Rh}$ , respectively. Note that the hybrid TAC model calculations have been performed for  $^{105}\text{Rh}$  and a smaller critical frequency  $\hbar\omega_{\text{crit}} = 0.20$  MeV was found [8]. For the higher  $\hbar\omega$ , a potential barrier appears around  $\varphi = 0$  and increases rapidly. The higher and wider barrier of the Routhian indicate a stronger suppressed tunneling between the left- and right-handed configurations and a stronger degeneracy of the chiral doublet bands [56] (cf. Fig. 6).

In order to visualize the chiral geometry, the self-consistently obtained orientation angles  $\theta$  and  $\varphi$  of the total angular momentum  $\mathbf{J}$  in the intrinsic frame are shown as functions of the rotational frequency  $\hbar\omega$  in Fig. 2. For the azimuthal angle, only the results of  $\varphi \geq 0$  are shown. The polar angle  $\theta$  behaves in a similar way for  $^{102-106}\text{Rh}$ , i.e., they increase with the rotational frequency. The  $\theta$  for  $^{107}\text{Rh}$  shows a decreasing behavior at low rotational frequency. As we can see below, this is due to the smaller and larger increments of ( $gd$ ) neutron angular momentum components along the  $s$  and  $l$  axes (cf. Fig. 5). Nevertheless, all of them are larger than  $45^\circ$ . This is attributed to that the angular momentum alignment along the  $s$ -axis coming from the neutron particle in the  $h_{11/2}$  shell is much larger than that along the  $l$  axis from the proton hole in the  $g_{9/2}$  shell. For comparison, the azimuth angle  $\varphi$  for  $^{103-107}\text{Rh}$  vanishes at low frequencies, corresponding to the planar rotation in the  $sl$  plane. Above the critical frequency  $\omega_{\text{crit}}$  (as discussed in Fig. 1), however, the  $\varphi$  values become

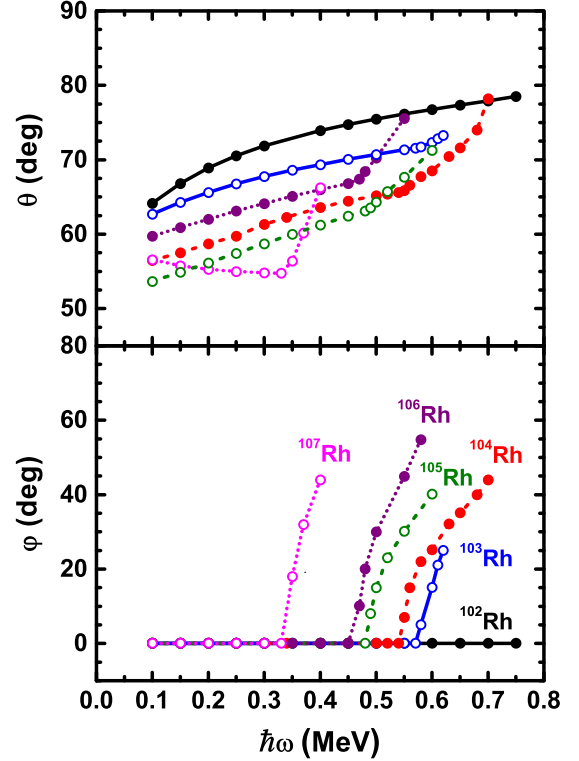


FIG. 2. Evolution of the orientation angles  $\theta$  and  $\varphi$  for the total angular momentum  $\mathbf{J}$  as driven by the increasing rotational frequency  $\hbar\omega$  for configurations  $\pi g_{9/2}^{-3} \otimes \nu[h_{11/2}^1(gd)^n]$  in  $^{102-107}\text{Rh}$ .

nonzero and results in the transition from planar to aplanar rotation. Note that there appears the kinks at the curves of  $\theta(\hbar\omega)$  for  $^{103-107}\text{Rh}$  at the critical frequency.

Furthermore, there is no nonzero value of  $\varphi$  for  $^{102}\text{Rh}$  even the rotational frequency goes up to  $\hbar\omega = 0.75$  MeV. The calculation could not be followed successfully up to  $\hbar\omega > 0.75$  MeV region. By further increasing  $\hbar\omega$ , convergent results can not be obtained for the configuration  $\pi g_{9/2}^{-3} \otimes \nu[h_{11/2}^1(gd)^6]$ . Namely, it might imply that  $\hbar\omega_{\text{crit}}$  for  $^{102}\text{Rh}$  in the present 3D-TAC CDFT calculation is larger than  $\hbar\omega = 0.75$  MeV, which corresponds to  $I \approx 20\hbar$  and is out of the spin range observed currently [11]. Therefore, the present theoretical analysis do not support static chirality in  $^{102}\text{Rh}$ , but cannot rule out the chiral vibration, which could be formed by the angular momentum  $\mathbf{J}$  in the  $sl$  plane ( $\varphi = 0$ ) by oscillating into the left and right sectors back and forth with slightly larger energy [16]. These features are consistent with previous study [11].

Therefore, the calculated critical frequency  $\omega_{\text{crit}}$  decreases with the increasing mass number for  $^{102-107}\text{Rh}$ , which can be supported by the behaviors of experimental spin-rotational frequency  $I(\hbar\omega)$  relationship. As shown in Fig. 3, the calculated values of  $I(\hbar\omega)$  agree well with the experimental data for  $^{103,105,106}\text{Rh}$ , though overestimate the data for  $^{102,104}\text{Rh}$ . We understand this as the number of valence of ( $gd$ ) neutrons in  $^{102,104}\text{Rh}$  is even and the pairing correlations, which are not considered here, may play more important roles. Furthermore, the calculated and experimental rotational frequencies  $\hbar\omega$  for

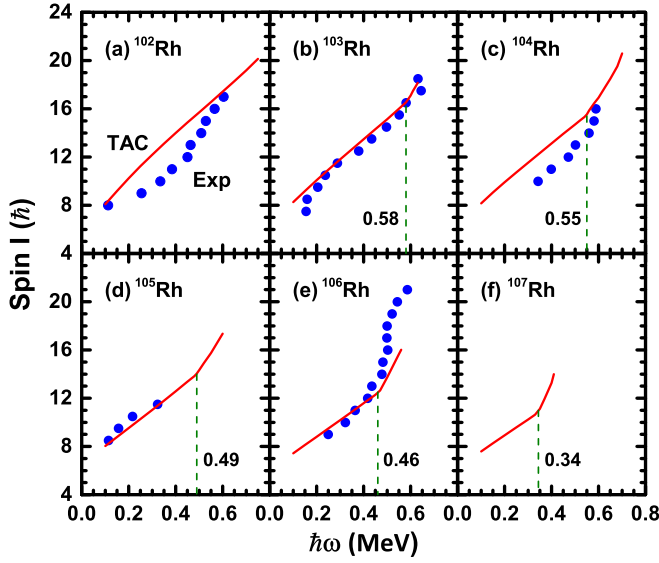


FIG. 3. The angular momenta as functions of rotational frequency  $\hbar\omega$  for the configurations  $\pi g_{9/2}^{-3} \otimes \nu[h_{11/2}^1(gd)^n]$  by 3D-TAC CDFT in comparisons with the available experimental data [5–8,10,11,15] in  $^{102-107}\text{Rh}$ .

the yrast bands for  $^{103-106}\text{Rh}$  behave very similarly with respect to the angular momentum. The bands in the low spin region show up as a nearly straight line. A kink appears at the critical frequency  $\omega_{\text{crit}}$  for  $^{103-106}\text{Rh}$ , due to the transition from the planar to the chiral solutions. The corresponding kink of experimental  $I(\hbar\omega)$  appears at almost the same as the calculated  $\hbar\omega_{\text{crit}}$  results for  $^{103,104,106}\text{Rh}$ . Further experimental efforts for  $^{105,107}\text{Rh}$  are encouraged to verify the present conclusion on the  $\hbar\omega_{\text{crit}}$ . For  $^{102}\text{Rh}$ , previous experimental investigation does not support static chirality interpretation in the spin range observed [11], which is in line with the theoretical result of no kink appearing.

Furthermore, the quasiparticle alignments for the yrast band in  $^{102-107}\text{Rh}$  have been extracted and shown in Fig. 4 in comparison with 3D-TAC CDFT results. The inspection of the alignments reveals that the yrast bands have  $\approx 7\hbar$  for  $^{102-105}\text{Rh}$  and  $\approx 6\hbar$  for  $^{106-107}\text{Rh}$ . The calculated quasiparticle alignments agree well with the experimental data for  $^{103,105,106}\text{Rh}$ , while overestimate the data for  $^{102,104}\text{Rh}$ , which is consistent with a previous study on the  $I(\hbar\omega)$  relationship and further validates the rationality of assigned configurations  $\pi g_{9/2}^{-3} \otimes \nu[h_{11/2}^1(gd)^n]$ . Considering that the valence nucleon configurations are kept unchanged with rotation, the continuous curves instead of the step-type one for quasiparticle alignments indicate that the kinks of  $I(\hbar\omega)$  shown in Fig. 3 are mainly originated from the appearance of aplanar rotation instead of quasiparticle alignment.

As is known, the chirality in nuclei having stable triaxial deformation is due to the aplanar rotation formed by the valence particle(s), valence hole(s), and collective core angular momentum vectors [1]. Therefore, an important focus is the transition point from the planar to the chiral rotation, i.e., the critical frequency  $\omega_{\text{crit}}$  [2]. As discussed above,  $\hbar\omega_{\text{crit}}$  decreases from  $\hbar\omega = 0.58$  MeV to 0.34 MeV with the

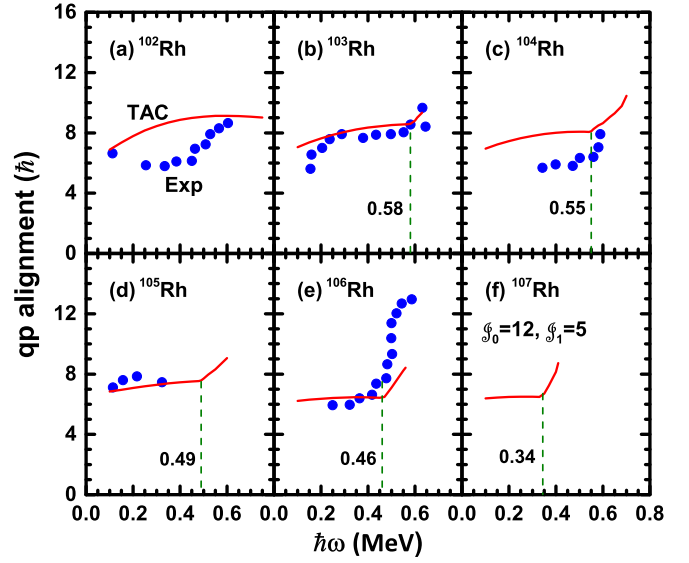


FIG. 4. Quasiparticle alignments as functions of rotational frequency  $\hbar\omega$  for the configurations  $\pi g_{9/2}^{-3} \otimes \nu[h_{11/2}^1(gd)^n]$  by 3D-TAC CDFT in comparisons with the available experimental data [5–8,10,11,15] in  $^{102-107}\text{Rh}$ . The Harris parameters used are  $\mathcal{J}_0 = 12 \hbar^2/\text{MeV}$  and  $\mathcal{J}_1 = 5 \hbar^4/\text{MeV}^3$ .

increasing mass number from 103 to 107. If  $\hbar\omega_{\text{crit}}$  existed in  $^{102}\text{Rh}$ , it was higher than  $\hbar\omega = 0.75$  MeV. To understand this interesting behavior, one has to analyze the underlying angular momentum geometry. In a self-consistent and microscopic calculation, all of nucleons are treated on the same footing and the total angular momentum comes from the individual nucleons in a coherent superposition manner. For all the rhodium isotopes in question, a neutron occupying at the bottom of the  $h_{11/2}$  shell contributes an angular momentum of roughly  $5.5\hbar$  along the  $s$  axis. In contrast, three proton holes locating at the top of the  $g_{9/2}$  shell contribute about  $3.5\hbar$  to the angular momentum along the  $l$  axis since two of them are antialigned. The only difference is the neutrons distributed over the  $(gd)$  orbitals above  $N = 50$  full shell and results in different configurations  $\pi g_{9/2}^{-3} \otimes \nu[h_{11/2}^1(gd)^n]$  ( $n = 6, 7, 8, 9, 10, \text{ and } 11$ ) for  $^{102-107}\text{Rh}$ . Therefore, to study how the  $(gd)$  neutrons influence the critical frequency  $\omega_{\text{crit}}$ , we extract the angular momentum contributions of the neutrons in the  $(gd)$  shells along the  $s$ ,  $m$ , and  $l$  axes and show them as functions of rotational frequency  $\hbar\omega$  in Fig. 5.

Figure 5 shows that the  $(gd)$  neutrons are characteristic of the particle, which contributes the angular momentum mainly along the  $s$  axis. The contributions of  $(gd)$  neutrons enlarge the asymmetric degree of configurations and the rotation mode favors the planar angular momentum geometry within the  $sl$  plane instead of the traditional chiral geometry. With increasing  $\hbar\omega$ , the increment of the angular momentum along the  $s$  axis is much larger than that along the  $l$  axis for  $^{102-106}\text{Rh}$ , while the increments are similar for  $^{107}\text{Rh}$  as a comparison. The increment of the angular momentum along the  $s$ -axis decreases with the neutron number and indicates the activity of  $(gd)$  neutrons declines. These  $(gd)$  neutrons contribute to the  $m$ -axis component above  $\hbar\omega_{\text{crit}}$  for  $^{103-107}\text{Rh}$ .

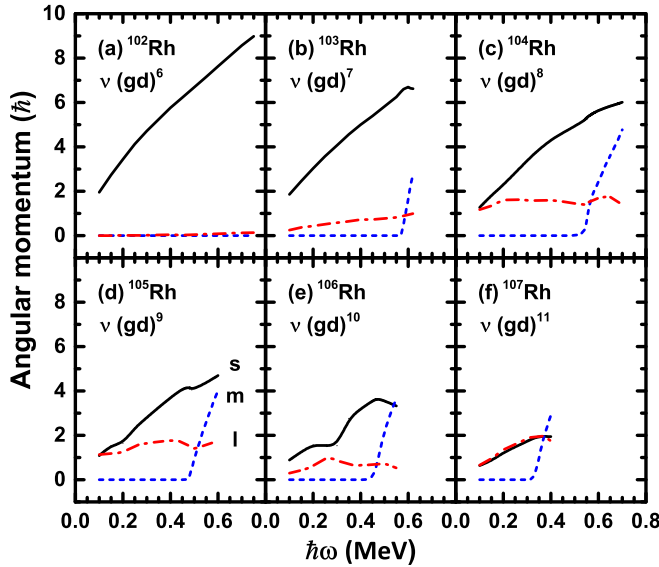


FIG. 5. Contributions of the neutrons in the  $(gd)^n$  shells to the neutron angular momentum along the short (solid lines), medium (dot-dashed lines), and long (dashed lines) axes for the configurations  $\pi g_{9/2}^{-3} \otimes \nu [h_{11/2}^1 (gd)^n]$  in  $^{102-107}\text{Rh}$  calculated by 3D-TAC CDFT.

In a short, the smaller increments of the angular momentum along the  $s$  axis and larger increments along the  $m$  axis from  $(gd)$  neutrons make it easier to form the aplanar rotation, and as a consequence reduce the corresponding critical frequency  $\omega_{\text{crit}}$ .

As aforementioned, the chiral candidates have been observed in  $^{102-106}\text{Rh}$  in the previous works [5–8,10,11,15].

The comparisons between the 3D-TAC CDFT results and the available experimental data [5–8,10,11,15] are shown in Fig. 6. The excitation energies and electromagnetic transition probabilities of the possible chiral bands in these nuclei are compared with the calculated results based on  $\pi g_{9/2}^{-3} \otimes \nu [h_{11/2}^1 (gd)^n]$  for  $^{102-107}\text{Rh}$ . Considering the fact that neither the chiral vibrations nor the quantum tunneling effect is taken into account in the present mean-field level, the energy splitting between the chiral doublet bands cannot be calculated. Therefore, only the experimental energy spectra of the yrast bands are reproduced by the 3D-TAC CDFT as shown in Fig. 6(a)–6(f). The quality of the present reproduction is reasonable since the calculations are free of additional parameters. Certainly, the pairing correlations are necessary to achieve a better description for the low spin region as shown in Ref. [55]. The description of the side bands is beyond the mean field. Further extensions, such as the random phase approximation [57,58] or the collective Hamiltonian [56,59,60], are necessary.

Since the experimental energy spectra of the side bands for  $^{102-106}\text{Rh}$  could not be reproduced by the 3D-TAC CDFT, only the experimental energy splitting are shown in Fig. 6(g)–6(k). The energy differences for  $^{103,104,106}\text{Rh}$  are close to the typical value 200–300 keV of chiral doublet bands [4]. The maximum of  $\Delta E$  for  $^{105}\text{Rh}$  is  $\approx 650$  keV, and the minimum of  $\Delta E$  for  $^{102}\text{Rh}$  is  $\approx 460$  keV. For the latter,  $^{102}\text{Rh}$ , previous experimental investigation does not suggest the static chirality interpretation in the spin range observed [11].

In Fig. 6(m)–6(r), the available data of  $B(M1)/B(E2)$  of chiral bands in  $^{102-107}\text{Rh}$  are displayed in comparison with the 3D-TAC CDFT results, which are derived in the semiclassical approximation from the magnetic and quadrupole

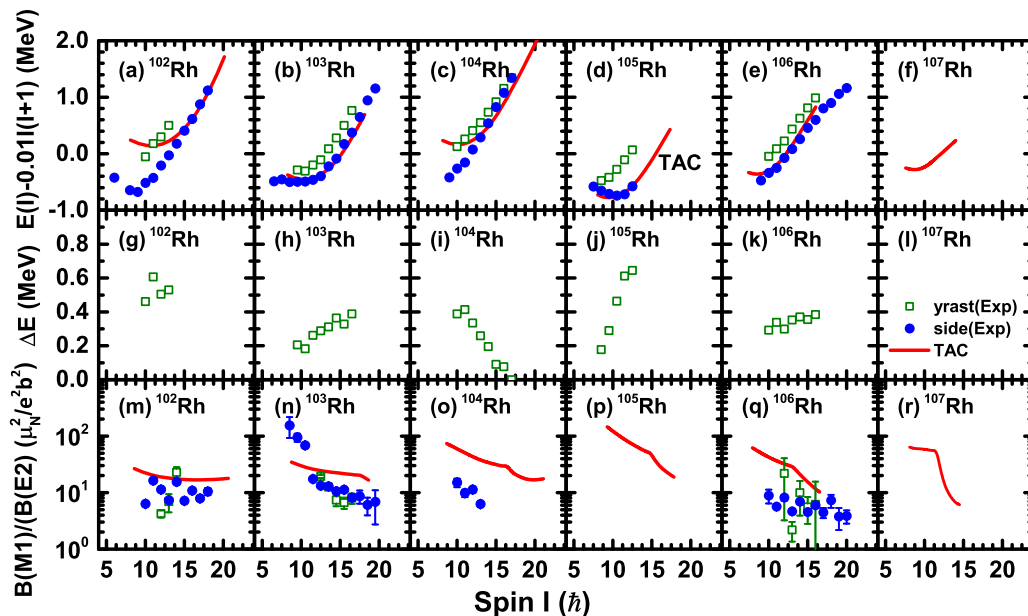


FIG. 6. The calculated results for the configurations  $\pi g_{9/2}^{-3} \otimes \nu [h_{11/2}^1 (gd)^n]$  by 3D-TAC CDFT in comparisons with the available experimental data [5–8,10,11,15] of doublet bands in  $^{102-107}\text{Rh}$ : (a)–(f) Energy spectra with respect to a common rigid rotor contribution. (g)–(k) Experimental energy differences between the doublet bands. (l) no experimental energy difference is available in  $^{107}\text{Rh}$ . (m)–(r)  $B(M1)/B(E2)$  ratios.

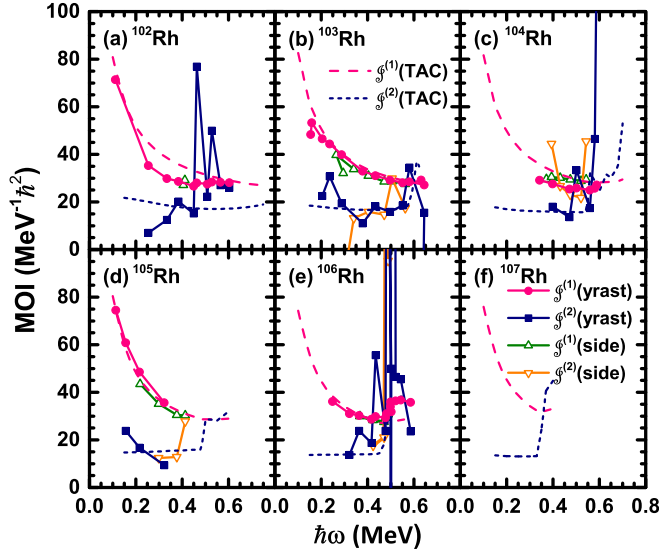


FIG. 7. The kinetic  $\mathcal{J}^{(1)}$  and dynamic  $\mathcal{J}^{(2)}$  moments of inertia (MOI) as functions of the rotational frequency  $\hbar\omega$  for the configurations  $\pi g_{9/2}^{-3} \otimes \nu[h_{11/2}(gd)^n]$  by 3D-TAC CDFT in comparisons with the available experimental data [5–8,10,11,15] of doublet bands in  $^{102-107}\text{Rh}$ .

moments [1]. In particular, the magnetic moments are derived from the relativistic expression of the effective current operator as in Refs. [30–32]. As shown in Fig. 6(m)–6(r), the 3D-TAC CDFT results for  $^{102}\text{Rh}$ ,  $^{103}\text{Rh}$ , and  $^{106}\text{Rh}$  show good agreements with the data within the error bar, while the calculation overestimates the data for  $^{104}\text{Rh}$ . The theoretical results show a smooth-falling behavior in the planar rotation, and the falling tendency slows down above  $\hbar\omega_{\text{crit}}$ . The falling tendency shows steeper and steeper with increasing neutron number. Further efforts of including the pairing correlations will be helpful to justify the present results.

In Fig. 7, the kinetic  $\mathcal{J}^{(1)}$  and dynamic  $\mathcal{J}^{(2)}$  moments of inertia are shown as functions of the rotational frequency  $\hbar\omega$  and compared with the data. In the present doublet bands, states differing by one unit of angular momentum are arranged into a pair of nearly degenerate  $\Delta I = 1$  bands. Therefore, the experimental values of kinetic  $\mathcal{J}^{(1)}$  and dynamic  $\mathcal{J}^{(2)}$  moments of inertia are calculated from the transition energies by using the finite-difference approximation for  $\Delta I = 1$  band,

$$\mathcal{J}^{(1)} = \frac{2I}{E_\gamma(I+1 \rightarrow I) + E_\gamma(I \rightarrow I-1)}, \quad (2)$$

$$\mathcal{J}^{(2)} = \frac{2}{E_\gamma(I+1 \rightarrow I) - E_\gamma(I-1 \rightarrow I-2)} \quad (3)$$

with  $\hbar\omega_{\text{exp}} = \frac{1}{2}[E_\gamma(I+1 \rightarrow I) + E_\gamma(I \rightarrow I-1)]$ . For  $\mathcal{J}^{(1)}$ , the experimental data for side bands are quite similar to the data for yrast bands, which are well reproduced by the 3D-TAC CDFT calculations for  $^{103,105,106}\text{Rh}$  while are overestimated by calculation for  $^{102,104}\text{Rh}$  due to the lack of pairing correlations. For  $\mathcal{J}^{(2)}$ , the 3D-TAC CDFT results change smoothly with rotational frequency  $\hbar\omega$ , and reproduce the

data in some observed  $\hbar\omega$  range well. The experimental data for yrast and side bands are alike in some observed spin range, and they are oscillating with rotational frequency. This may come from the configuration mixing with the normal deformed band [61]. Furthermore, the calculated values for  $\mathcal{J}^{(1)}$  and  $\mathcal{J}^{(2)}$  are closer and closer to each other with the rotating and become rather similar above the critical frequency  $\omega_{\text{crit}}$ .

#### IV. SUMMARY

In summary, a fully self-consistent and microscopic investigation for three-dimensional rotation and chirality in the rhodium isotopes  $^{102-107}\text{Rh}$  has been carried with the 3DTAC CDFT with the configurations  $\pi g_{9/2}^{-3} \otimes \nu[h_{11/2}(gd)^n]$ .

A transition from the planar to the chiral rotation has been found for  $^{103-107}\text{Rh}$ , whereas only planar solution has been confirmed for  $^{102}\text{Rh}$  up to  $\hbar\omega = 0.75$  MeV. The evolution of the orientation angles  $\theta$  and  $\varphi$  for the rotational frequency in  $^{102-107}\text{Rh}$  have been investigated. The critical frequency  $\omega_{\text{crit}}$  decreases with increasing neutron number, which is supported partly by the existing experimental data of  $^{103,104,106}\text{Rh}$  and is still needed to be verified based on the future experimental efforts for  $^{105,107}\text{Rh}$ . The contributions of the neutrons in the  $(gd)$  shells to the neutron angular momenta along the  $s$ ,  $m$ , and  $l$  axes are extracted and found that they indeed affect the appearance of the aplanar rotation and the corresponding critical frequency  $\omega_{\text{crit}}$ . The smaller increments of the angular momentum along the  $s$  axis and larger increments along the  $m$  axis from  $(gd)$  neutrons make it easier to form the aplanar rotation, and as a consequence reduce the corresponding critical frequency  $\omega_{\text{crit}}$ .

The calculated energy spectra for yrast bands of  $^{102-105}\text{Rh}$  are reasonable with the corresponding experimental data. The kinetic moments of inertia  $\mathcal{J}^{(1)}$  of the yrast band are well reproduced by the 3D-TAC CDFT calculations for  $^{103,105,106}\text{Rh}$ , while are overestimated by a calculation for  $^{102,104}\text{Rh}$ . The 3D-TAC CDFT results of dynamic moments of inertia  $\mathcal{J}^{(2)}$  change smoothly with rotational frequency  $\hbar\omega$  and reproduce the data, which show oscillations with rotational frequency, on part of the  $\hbar\omega$  range. The 3D-TAC CDFT results show a good agreement with the data of  $B(M1)/B(E2)$  for  $^{102}\text{Rh}$ ,  $^{103}\text{Rh}$ , and  $^{106}\text{Rh}$ , while overestimates the data for  $^{104}\text{Rh}$ .

Further efforts of including the pairing correlations and beyond mean field effects in the calculations will be helpful to justify the present results and understand the underlying rotational structure in these rhodium nuclei.

#### ACKNOWLEDGMENTS

The authors thank P. W. Zhao for providing the numerical code of 3D-TAC CDFT. This work is supported by the National Natural Science Foundation of China (NSFC) under Grants No. 11775026 and 11875027. This research was supported by the Super Computing Center of Beijing Normal University.

- [1] S. Frauendorf and J. Meng, *Nucl. Phys. A* **617**, 131 (1997).
- [2] P. Olbratowski, J. Dobaczewski, J. Dudek, and W. Płóciennik, *Phys. Rev. Lett.* **93**, 052501 (2004).
- [3] J. Meng, J. Peng, S. Q. Zhang, and S.-G. Zhou, *Phys. Rev. C* **73**, 037303 (2006).
- [4] B. W. Xiong and Y. Y. Wang, *At. Data Nucl. Data Tables* **125**, 193 (2019).
- [5] C. Vaman, D. B. Fossan, T. Koike, K. Starosta, I. Y. Lee, and A. O. Macchiavelli, *Phys. Rev. Lett.* **92**, 032501 (2004).
- [6] P. Joshi, D. G. Jenkins, P. M. Raddon, A. J. Simons, R. Wadsworth, A. R. Wilkinson, D. B. Fossan, T. Koike, K. Starosta, C. Vaman, J. Timár, Zs. Dombrádi, A. Krasznahorkay, J. Molnár, D. Sohler, L. Zolnai, A. Algora, E. S. Paul, G. Rainovski, A. Gizon *et al.*, *Phys. Lett. B* **595**, 135 (2004).
- [7] J. Timár, C. Vaman, K. Starosta, D. B. Fossan, T. Koike, D. Sohler, I. Y. Lee, and A. O. Macchiavelli, *Phys. Rev. C* **73**, 011301(R) (2006).
- [8] J. A. Alcántara-Núñez, J. R. B. Oliveira, E. W. Cybulska, N. H. Medina, M. N. Rao, R. V. Ribas, M. A. Rizzutto, W. A. Seale, F. Falla-Sotelo, K. T. Wiedemann, V. I. Dimitrov, and S. Frauendorf, *Phys. Rev. C* **69**, 024317 (2004).
- [9] J. Timár, P. Joshi, K. Starosta, V. I. Dimitrov, D. B. Fossan, J. Molnár, D. Sohler, R. Wadsworth, A. Algora, P. Bednarczyk, D. Curien, Zs. Dombrádi, G. Duchene, A. Gizon, J. Gizon, D. G. Jenkins, T. Koike, A. Krasznahorkay, E. S. Paul, P. M. Raddon *et al.*, *Phys. Lett. B* **598**, 178 (2004).
- [10] T. Suzuki, G. Rainovski, T. Koike, T. Ahn, M. P. Carpenter, A. Costin, M. Danchev, A. Dewald, R. V. F. Janssens, P. Joshi, C. J. Lister, O. Möller, N. Pietralla, T. Shinozuka, J. Timár, R. Wadsworth, C. Vaman, and S. Zhu, *Phys. Rev. C* **78**, 031302(R) (2008).
- [11] D. Tonev, M. S. Yavahchova, N. Goutev, G. de Angelis, P. Petkov, R. K. Bhowmik, R. P. Singh, S. Muralithar, N. Madhavan, R. Kumar, M. Kumar Raju, J. Kaur, G. Mohanto, A. Singh, N. Kaur, R. Garg, A. Shukla, Ts. K. Marinov, and S. Brant, *Phys. Rev. Lett.* **112**, 052501 (2014).
- [12] C. Droste, S. G. Rohozinski, K. Starosta, L. Prochniak, and E. Grodner, *Eur. Phys. J. A* **42**, 79 (2009).
- [13] Q. B. Chen, J. M. Yao, S. Q. Zhang, and B. Qi, *Phys. Rev. C* **82**, 067302 (2010).
- [14] I. Hamamoto, *Phys. Rev. C* **88**, 024327 (2013).
- [15] I. Kuti, Q. B. Chen, J. Timár, D. Sohler, S. Q. Zhang, Z. H. Zhang, P. W. Zhao, J. Meng, K. Starosta, T. Koike, E. S. Paul, D. B. Fossan, and C. Vaman, *Phys. Rev. Lett.* **113**, 032501 (2014).
- [16] V. I. Dimitrov, S. Frauendorf, and F. Döna, *Phys. Rev. Lett.* **84**, 5732 (2000).
- [17] V. I. Dimitrov, F. Donau, and S. Frauendorf, *Phys. Rev. C* **62**, 024315 (2000).
- [18] J. Peng, J. Meng, and S. Q. Zhang, *Phys. Rev. C* **68**, 044324 (2003).
- [19] S. Y. Wang, S. Q. Zhang, B. Qi, J. Peng, J. M. Yao, and J. Meng, *Phys. Rev. C* **77**, 034314 (2008).
- [20] B. Qi, S. Q. Zhang, S. Y. Wang, J. Meng, and T. Koike, *Phys. Rev. C* **83**, 034303 (2011).
- [21] J. Peng, H. Sagawa, S. Q. Zhang, J. M. Yao, Y. Zhang, and J. Meng, *Phys. Rev. C* **77**, 024309 (2008).
- [22] J. M. Yao, B. Qi, S. Q. Zhang, J. Peng, S. Y. Wang, and J. Meng, *Phys. Rev. C* **79**, 067302 (2009).
- [23] J. Li, S. Q. Zhang, and J. Meng, *Phys. Rev. C* **83**, 037301 (2011).
- [24] A. D. Ayangeakaa, U. Garg, M. D. Anthony, S. Frauendorf, J. T. Matta, B. K. Nayak, D. Patel, Q. B. Chen, S. Q. Zhang, P. W. Zhao, B. Qi, J. Meng, R. V. F. Janssens, M. P. Carpenter, C. J. Chiara, F. G. Kondev, T. Lauritsen, D. Seweryniak, S. Zhu, S. S. Ghugre *et al.*, *Phys. Rev. Lett.* **110**, 172504 (2013).
- [25] C. Liu, S. Y. Wang, R. A. Bark, S. Q. Zhang, J. Meng, B. Qi, P. Jones, S. M. Wyngaardt, J. Zhao, C. Xu, S.-G. Zhou, S. Wang, D. P. Sun, L. Liu, Z. Q. Li, N. B. Zhang, H. Jia, X. Q. Li, H. Hua, Q. B. Chen *et al.*, *Phys. Rev. Lett.* **116**, 112501 (2016).
- [26] C. M. Petrache, B. F. Lv, A. Astier, E. Dupont, Y. K. Wang, S. Q. Zhang, P. W. Zhao, Z. X. Ren, J. Meng, P. T. Greenlees, H. Badran, D. M. Cox, T. Grahn, R. Julin, S. Juutinen, J. Konki, J. Pakarinen, P. Papadakis, J. Partanen, P. Rahkila *et al.*, *Phys. Rev. C* **97**, 041304(R) (2018).
- [27] T. Roy, G. Mukherjee, Md. A. Asgar, S. Bhattacharyya, S. Bhattacharya, C. Bhattacharya, S. Bhattacharya, T. K. Ghosh, K. Banerjee, S. Kundu, T. K. Rana, P. Roy, R. Pandey, J. Meena, A. Dhal, R. Palit, S. Saha, J. Sethi, S. Thakur, B. S. Naidu *et al.*, *Phys. Lett. B* **782**, 768 (2018).
- [28] B. F. Lv, C. M. Petrache, Q. B. Chen, J. Meng, A. Astier, E. Dupont, P. Greenlees, H. Badran, T. Calverley, D. M. Cox, T. Grahn, J. Hilton, R. Julin, S. Juutinen, J. Konki, J. Pakarinen, P. Papadakis, J. Partanen, P. Rahkila, P. Ruotsalainen *et al.*, *Phys. Rev. C* **100**, 024314 (2019).
- [29] C. M. Petrache, B. F. Lv, Q. B. Chen, J. Meng, A. Astier, E. Dupont, K. K. Zheng, P. T. Greenlees, H. Badran, T. Calverley, D. M. Cox, T. Grahn, J. Hilton, R. Julin, S. Juutinen, J. Konki, J. Pakarinen, P. Papadakis, J. Partanen, P. Rahkila *et al.*, *Eur. Phys. J. A* **56**, 208 (2020).
- [30] P. W. Zhao, *Phys. Lett. B* **773**, 1 (2017).
- [31] P. W. Zhao, Y. K. Wang, and Q. B. Chen, *Phys. Rev. C* **99**, 054319 (2019).
- [32] J. Peng and Q. B. Chen, *Phys. Lett. B* **810**, 135795 (2020).
- [33] P.-G. Reinhard, *Rep. Prog. Phys.* **52**, 439 (1989).
- [34] P. Ring, *Prog. Part. Nucl. Phys.* **37**, 193 (1996).
- [35] B. Serot and J. D. Walecka, *Int. J. Mod. Phys. E* **06**, 515 (1997).
- [36] D. Vretenar, A. V. Afanasjev, G. A. Lalazissis, and P. Ring, *Phys. Rep.* **409**, 101 (2005).
- [37] J. Meng, H. Toki, S. Zhou, S. Zhang, W. Long, and L. Geng, *Prog. Part. Nucl. Phys.* **57**, 470 (2006).
- [38] J. Meng (ed.), *Relativistic Density Functional for Nuclear Structure*, Vol. 10 of International Review of Nuclear Physics (World Scientific, Singapore, 2016).
- [39] J. König and P. Ring, *Phys. Rev. Lett.* **71**, 3079 (1993).
- [40] H. Madokoro, J. Meng, M. Matsuzaki, and S. Yamaji, *Phys. Rev. C* **62**, 061301(R) (2000).
- [41] J. Peng, J. Meng, P. Ring, and S. Q. Zhang, *Phys. Rev. C* **78**, 024313 (2008).
- [42] P. W. Zhao, S. Q. Zhang, J. Peng, H. Z. Liang, P. Ring, and J. Meng, *Phys. Lett. B* **699**, 181 (2011).
- [43] L. F. Yu, P. W. Zhao, S. Q. Zhang, P. Ring, and J. Meng, *Phys. Rev. C* **85**, 024318 (2012).
- [44] J. Meng, J. Peng, S. Q. Zhang, and P. W. Zhao, *Front. Phys.* **8**, 55 (2013).
- [45] J. Meng and P. W. Zhao, *Phys. Scr.* **91**, 053008 (2016).
- [46] P. W. Zhao, J. Peng, H. Z. Liang, P. Ring, and J. Meng, *Phys. Rev. Lett.* **107**, 122501 (2011).
- [47] P. W. Zhao, J. Peng, H. Z. Liang, P. Ring, and J. Meng, *Phys. Rev. C* **85**, 054310 (2012).
- [48] J. Peng and P. W. Zhao, *Phys. Rev. C* **91**, 044329 (2015).
- [49] J. Li, *Phys. Rev. C* **97**, 034306 (2018).

- [50] B. Qi, H. Jia, C. Liu, and S. Y. Wang, *Phys. Rev. C* **98**, 014305 (2018).
- [51] J. Peng and Q. B. Chen, *Phys. Rev. C* **98**, 024320 (2018).
- [52] P. W. Zhao, Z. P. Li, J. M. Yao, and J. Meng, *Phys. Rev. C* **82**, 054319 (2010).
- [53] P. Olbratowski, J. Dobaczewski, and J. Dudek, *Phys. Rev. C* **73**, 054308 (2006).
- [54] S. Frauendorf, *Nucl. Phys. A* **677**, 115 (2000).
- [55] P. W. Zhao, S. Q. Zhang, and J. Meng, *Phys. Rev. C* **92**, 034319 (2015).
- [56] Q. B. Chen, S. Q. Zhang, P. W. Zhao, R. V. Jolos, and J. Meng, *Phys. Rev. C* **87**, 024314 (2013).
- [57] S. Mukhopadhyay, D. Almeded, U. Garg, S. Frauendorf, T. Li, P. V. Madhusudhana Rao, X. Wang, S. S. Ghughre, M. P. Carpenter, S. Gros, A. Hecht, R. V. F. Janssens, F. G. Kondev, T. Lauritsen, D. Seweryniak, and S. Zhu, *Phys. Rev. Lett.* **99**, 172501 (2007).
- [58] D. Almeded, F. Dönau, and S. Frauendorf, *Phys. Rev. C* **83**, 054308 (2011).
- [59] Q. B. Chen, S. Q. Zhang, P. W. Zhao, R. V. Jolos, and J. Meng, *Phys. Rev. C* **94**, 044301 (2016).
- [60] X. H. Wu, Q. B. Chen, P. W. Zhao, S. Q. Zhang, and J. Meng, *Phys. Rev. C* **98**, 064302 (2018).
- [61] E. Ideguchi, D. G. Sarantites, W. Reviol, A. V. Afanasjev, M. Devlin, C. Baktash, R. V. F. Janssens, D. Rudolph, A. Axelsson, M. P. Carpenter, A. Galindo-Uribarri, D. R. LaFosse, T. Lauritsen, F. Lerma, C. J. Lister, P. Reiter, D. Seweryniak, M. Weiszflog, and J. N. Wilson, *Phys. Rev. Lett.* **87**, 222501 (2001).